

Pulmonary acini exhibit complex changes during postnatal rat lung development

This manuscript ([permalink](#)) was automatically generated from [habi/acinar-analysis-manuscript@ccc52be](#) on December 1, 2020.

Authors

- **David Haberthür**

 [0000-0003-3388-9187](#) ·  [habi](#) ·  [habi](#)

Institute of Anatomy, University of Bern, Switzerland · Funded by Swiss National Science Foundation (Schweizerische Nationalfonds) <http://p3.snf.ch/project-153468>; Swiss National Science Foundation (Schweizerische Nationalfonds) <http://p3.snf.ch/project-175953>

- **Eveline Yao**

Institute of Anatomy, University of Bern, Switzerland

- **Sébastien F. Barré**


Institute of Anatomy, University of Bern, Switzerland · Funded by Swiss National Science Foundation (Schweizerische Nationalfonds) 153468; Swiss National Science Foundation (Schweizerische Nationalfonds) 175953

- **Tiziana P. Cremona**

 [0000-0003-0061-9578](#)

Institute of Anatomy, University of Bern, Switzerland · Funded by Swiss National Science Foundation (Schweizerische Nationalfonds) 153468; Swiss National Science Foundation (Schweizerische Nationalfonds) 175953

- **Stefan A. Tschanz**

 [0000-0003-3880-4437](#)

Institute of Anatomy, University of Bern, Switzerland

- **Johannes C. Schittny**

 [0000-0003-4025-3961](#)

Institute of Anatomy, University of Bern, Switzerland · Funded by Swiss National Science Foundation (Schweizerische Nationalfonds) 153468; Swiss National Science Foundation (Schweizerische Nationalfonds) 175953

Abstract

Pulmonary acini exhibit complex changes during postnatal rat lung development David Haberthür¹ ,
Eveline Yao¹ , Sébastien F. Barré¹ , Tiziana P. Cremona¹ , Stefan A. Tschanz¹ , and Johannes C.
Schittny¹ ¹

University of Bern

April 23, 2020 ¹

Abstract

2

Pulmonary acini represent the functional gas-exchanging units of the lung. Due to technical
limitations, it is not possible to identify individual acini on microscopic lung sections.

3

8

We imaged instillation-fixed rat lungs at postnatal days P4, P10, P21, and P60 to overcome these
limitations. Right lower lobes of these lungs were imaged at the TOMCAT beamline of the Swiss Light
Source synchrotron facility at a voxel size of 1.48 μm . Individual acini ($N=268$) were segmented from
the 3D data by closing the airways ways at the transition point from conducting to gas exchanging
airways. Acinar development was followed by estimating the individual acinar volume, complexity,
and number of alveoli.

9

The mean volume of the acini increases 23 times during the observed timeframe. The coefficients of
variation dropped from

10

1.26 to 0.49 and the difference between the mean volumes of the fraction of the 20 % smallest to the
20 % largest acini decreased from a factor of 27.26 (day 4) to a factor of 4.07 (day 60), i.e. shows a
smaller dispersion at later time points.

4 5 6 7

11

13

This indicates that the acinar volumes show a very large variation at early timepoints and homogenize
during maturation of the lung. Our approach is well suited to follow acinar development and to
acquire stereologically correct data in a

14

time-efficient manner. We found that the newly formed acini show a large size distribution which is reduced by a factor of

15

7 until adulthood. Most likely this leads to a more homogeneous ventilation in the lung.

16

1

17

1.1

12

18 19 20 21 22 23 24 25 26 27 28 29 30 31 32 33 34

Introduction Lung development

Lung development starts with the formation of the two lung buds. During the embryonic stage (prenatal days E11-E13 in rats) the major airways and the pleura are formed. During the pseudoglandular stage (E13-E18.5) most of the remaining airway generations are formed by branching morphogenesis. Few additional branches are added during the canalicular (E18.5 - E20) and maybe the saccular stage (E20 to postnatal day P4). Epithelial differentiation becomes morphologically visible during the canalicular stage. Together with angiogenetic activation of the capillaries, this process leads to the first functional air-blood barriers in the lung. The saccular stage represents an intermediate stage where branching morphogenesis ceases and the developmental program switches to the phase of alveolarization. During alveolarization, 90 % of the adult gas-exchange area is formed by the lifting off of new septa from the existing gas-exchange surface (1; 2; 3). Alveolarization itself is divided into two distinct phases, the so-called classical (P4-P21) and continued alveolarization (P14 to approximately P60). During classical alveolarization, new septa are formed starting from preexisting immature septa which contain a double-layered capillary network. During alveolarization, the structure of the alveolar septa is changed to increase the efficiency of the lung. It includes the transformation of the double-layered capillary network into a single-layered one. As a consequence, angiogenesis is necessary at the basis of the newly forming septa. To distinguish these modes of the formation of new alveolar septa and to specify 1

39

that alveolarization continues after classical alveolarization ceased, the second phase of alveolarization is called continued alveolarization. Here, the timing of lung development is given for rats while the same stages and developmental mechanisms are observed in every placentalian species studied so far, including humans. However, the timing of lung development and especially the time point of birth relative to lung development is adapted in each species (3; 4; 5).

40

1.2

35 36 37 38

The functional lung units

Pulmonary acini represent the gas-exchanging units of the bronchial tree and are defined as the airways distal of the terminal bronchioles (6). In humans, the acini contain approximately four generations of respiratory bronchioles before reaching the alveolar ducts. The alveolar ducts start at the so-called bronchioalveolar duct junction (BADJ) where the lining of the inner airway surface abruptly changes from the cuboidal epithelium of the bronchioles into type 1 and type 2 alveolar epithelium which covers the alveoli. The small tree of airways distal of the BADJ is called a ventilatory unit (7). Since murine lungs do not possess respiratory bronchioles, the murine acini consist of one single ventilatory unit (7). In this study we used rat lungs; hence we exclusively speak of acini. To translate our results to humans, monkeys, or dogs, one would have to compare a rat acinus to a single ventilatory unit in these species. Developmentally, the BADJ is of particular interest. The junction is formed during the canalicular stage when the epithelia are differentiating. Ciliated epithelia containing goblet or club cells form proximal and type I and II alveolar epithelia form distal of the BADJ. The BADJ is home to various stem cells (7). The generation of the airway in which an individual murine acinus starts is defined during the canalicular stage and remains constant once it is formed. As a consequence, the number of formed acini also remains constant during the phase of alveolarization and thereafter (8; 9). The latter was somehow surprising because the total lung volume increases by roughly a factor of 10 during alveolarization (10). Therefore, the mean volume of the acini has to increase by approximately the same factor. Since the acinus volume can easily be estimated with the Cavalieri principle (11), we can test if and how the acinus volume increases during lung development.

68

However, besides the global numbers little is known about the range of the volume of individual acini throughout lung development. The latter represents a physiological significant value, because it has been shown by pulmonary particle deposition (12; 13; 10) and by computational fluid dynamics simulations of airflow (14; 15; 16) that the acinar architecture is important for ventilation and particle deposition. However, due to the lack of measured data, these simulations are based on acinar models. Therefore, the question of how well these models represent lung physiology remains open until the necessary data and physiologically correct models are available. To contribute to the validation of the computational fluid dynamics simulations, we determined the volume and number of alveoli in individual acini throughout rat lung development.

69

1.3

60 61 62 63 64 65 66 67

70 71 72 73 74 75 76 77 78 79 80 81 82 83

Acinus detection and delineation

To detect and delineate individual acini, three-dimensional information is needed. On single twodimensional (histological) sections it is not possible to unambiguously detect which parts of the airways and alveoli in the lung parenchyma are connected three-dimensionally. Historically, single or very few acini were delineated and extracted from manually traced serial sections (17; 18) or sectioned silicone casts (19), both with considerable manual work. Non-destructive three-dimensional imaging is best suited to acquire data sets that can be used to easily detect, delineate and study large amounts of single acini. This has been shown by Vasilescu et al. (20). In their study, they reconstructed

22 mouse acini from tomographic data sets of four 12 week old mice (at least postnatal day 84, fully developed lungs) and compared those with scanning electron microscope images of acinar silicone rubber casts. Similarly, Kizhakke Puliyakote et al. (21) analyzed the volume of 32 mouse acini from six animals, as well as the branching pattern of their internal airways. All prior work known to us has analyzed considerably fewer acini than the 268 acini presented in this manuscript and - due to the study design - focuses only on one time point, where the lungs of the animals are already fully developed while we are wable to analyze the acini over the course of postnatal lung development.

2

89

The hereby presented method is well adapted to thoroughly analyze large amounts of acini in a timeefficient manner. The largest part of the work is spent on the detailed stereological analysis of the extracted acini. The method makes it possible to provide data spanning relevant parts of the lung development in animals. As confirmed by Vasilescu et al. (22), stereologically analyzing microtomographic data provides quantitative information on internal structures of the lung while preserving the samples for further studies.

90

2

91

2.1

84 85 86 87 88

92 93 94 95 96 97 98 99 100 101 102 103

Materials & Methods Rat lung samples

In the present study, a superset of the animals described by Haberthür et al. (23) were used. Tschanz et al. (10) described a biphasic formation of new alveoli on the same set of animals. The stereological analysis presented here represents a part of the 3R-initiative (replacement, reduction, and refinement) (24) for the ethical use and the reduction of the number of animals sacrificed for science. Briefly, we extracted the lungs of Sprague-Dawley rats after having deeply anesthetized them with a mixture of medetomidine, midazolam, and fentanyl (25). The rats were euthanized by exsanguination during the removal of the lung. The lungs were fixed with 2.5 % glutaraldehyde by intratracheal instillation and kept under constant pressure (20 cm H₂ O) during fixation to prevent recoiling of the tissue. The samples were prepared for tomographic imaging by post-fixation with 1 % osmium tetroxide and staining with 4 % uranyl acetate, as well as by dehydration in a graded series of ethanol and embedding in paraffin. In total we assessed 12 animals, on postnatal days P4, P10, P21, and P60 (N=3 per day. From now on, we will omit the postnatal prefix and only mention the day.).

108

The animals were housed in the central animal facility of the University of Bern. They received food and water ad libitum at a 12/12 hours day/night cycle. The experiments themselves, as well as the handling of the animals before and during the experiments, were approved and supervised by the Federal Food Safety and Veterinary Office of Switzerland and the Department of Agriculture and Nature of the Kanton of Bern in Switzerland.

Tomographic imaging

Tomographic imaging was performed at the TOMCAT beamline (26; 27) of the Swiss Light Source at the Paul Scherrer Institute in Villigen, Switzerland. The samples were scanned at an X-ray energy of 20.0 keV. After penetrating the sample, the X-rays were converted into visible light by either a 20- μm -thick LuAG:Ce or 18- μm -thick YAG:Ce scintillator screen (both from Crytur, Turnov, Czech Republic), depending on the date of experiments. The resulting visible light was magnified using a 10times magnifying, diffraction-limited microscope lens and recorded with a 2048 \times 2048 pixel CCD camera (pco.2000, PCO, Kelheim, Germany) with 14 bits dynamic range operated in 2 by 2 binning mode. As a result, in a single field of view, we were able to image a sample volume of a cube of 1.5 mm side length with a voxel side length of 1.48 μm , with the exposure time of the single projections varying between 160 and 200 ms. Since our samples were substantially larger than the field of view of the detector, we applied the so-called wide-field scanning method (28) to increase the field of view horizontally. For each sub-scan, we recorded 3578 projections and laterally stitched them so that their combined field of view covered the whole sample width. Additionally, two or three such wide-field scans were stacked vertically to match the sample height. The resulting data sets for each of the lung samples covered a field of view of a cube with approximately 4.5 mm side length which corresponds to an image stack with approximately 3000 \times 3000 \times 3000 pixels at 1.48 μm side length each. The mean size of the tomographic reconstructions, corresponding to the raw data of each of the 42 analyzed tomographic scans is 8 GB, totaling to 336 GB.

Extraction of acini

For the present manuscript, we extracted single acini from three-dimensional data, acquired without destroying the samples. Details of this semi-automatic extraction of the rat acini are described by Haberthür et al. (23). We applied this protocol to extract 701 randomly selected acini throughout lung development, at postnatal days 4, 10, 21 and 60. Individual acini were extracted from the tomographic data with a custom image processing network established in MeVisLab (version 2.1, 2010-07-26 release, MeVis Medical Solutions and Fraunhofer MEVIS-Institute for Medical Image Computing, Bremen, Germany).

This extraction was performed by segmenting the acinus volume with a gray-level threshold-based region growing algorithm using manually placed seed points. To isolate individual acini in the data set we placed disk-shaped segmentation stoppers at the acinus entrances. Each individual acinus was then exported as a single DICOM file for portability. For each acinus, its exported DICOM file contained

the segmented acinus overlaid with the original background for further analysis. Example images from the DICOM files are shown in the bottom row of Fig 1.

143

2.4

137 138 139 140 141

144 145 146 147 148 149 150 151 152 153 154 155 156 157

Stereological analysis of alveolar characteristics

The stereological estimation of the alveolar number was performed according to the standards for quantitative assessment of lung structure from the American Thoracic Society (29) to guarantee accurate and unbiased results. To perform the stereological analysis, each DICOM file from the isolated acini was sampled into a systematic random set of single images using a MATLAB script (30). The stereological assessment was performed with the STEPanizer (31), an easy-to-use software tool for the stereological assessment of digital images. Details of the stereological assessment have previously been described (32). Briefly, we counted the appearance or disappearance of alveolar wall interruptions. Under the assumption that these only occur in the region of the alveolar mouth opening and correspond to alveolar entrance rings (33) we counted said interruptions on paired images spanning the whole acinus volume. By using the disector method (34) we were thus able to estimate the number of alveoli in 268 of the 701 exported acini. The acini we analyzed were subsampled from the full data by systematic uniform random sampling (35). Briefly, a defined fraction of the acini of one animal were analyzed, e.g. one third. During segmentation, the acini were numbered. Based on these numbers every third acinus was selected, randomly starting with the first, second, or third one.

164

Previously, we have shown that the stereological assessment of the acinar volume (according to the Cavalieri principle (36)) gives comparable results to an automated volume extraction by counting the segmented pixels in the tomographic data sets (32). Due to variations in the gray value, the automatic segmentation underestimates the volume of the single acini. The best-suited approach to obtain unbiased results is to assess the volume manually according to the Cavalieri principle, which is what we did for the 268 acini presented in this manuscript. The sets of JPG slices and the raw results from the stereological analysis with the STEPanizer are available on request.

165

2.5

158 159 160 161 162 163

166 167 168 169 170 171 172 173 174 175 176

Data analysis and display

All the stereologically assessed data was processed in a Jupyter (37) notebook, producing all the results, including the statistical data and plots shown below. The notebook with all its history is freely available on GitHub (38). The performed calculations are described in detail in section 3. In the plots, semitransparent circles mark the single observations. The box shows the 25-75 % quartiles range of

the data. The whiskers extend to the rest of the distribution. Outliers are determined as a function of the inter-quartile range and are shown outside the whiskers. Numerical values in the text are given as averages \pm standard deviation. P-values in the text and figure legends are given as precise numbers, as suggested by Amrhein et al. (39). Usually, we performed a Shapiro-Wilk test for normality (40) to test whether we can use an U-test for assessing the differences, namely a two-sided Mann-Whitney rank test (41). This rank test was used to assess the differences between the possible combinations. An additional Kruskal-Wallis H-test for independent samples (42) was used to test for sample independence. The statistical analysis was

4

178

performed in the aforementioned notebook by using the statistical functions of the Scientific Computing Tools for Python (43) or GraphPad Prism 7.01 (GraphPad Software, San Diego, CA, USA).

179

3

177

180 181 182 183 184 185 186

Results

The number of alveoli per acinus was assessed for 268 individual acini throughout postnatal lung development at days 4, 10, 21 and 60. For day 4, we analyzed 125 acini, for day 10 we analyzed 58 acini, for day 21 we analyzed 42 acini, and for day 60 we analyzed 43 acini. To get started, we show an overview of our process in figure 1. Panels A-D show a representative light microscopy image for each assessed time point. Panels E-H of figure 1 each correspond to one slice of the tomographic data sets acquired at TOMCAT. Panels I-L of figure 1 show the middle slice of the datasets used for the stereological analysis of the extracted acini. The acinus is shown in light gray as an overlay over the tomographic data.

Figure 1: Example images for each of the assessed time points. A-D: Representative light microscopy images. E-H: One slice of the tomographic data sets. I-L: Middle slice of one of the extracted acini. The extracted acinus is overlaid on the tomographic dataset. Panels J and K also show the segmentation stopper at the left border of the image. The shown images correspond to the middle slice of the full data sets used for the stereological analysis. The scale bar was burnt in during preparation of the image stacks and is 100 μ m long. Panels A, E & I: Day 4. Panels B, F & J: Day 10. Panels C, G & K: Day 21. Panels D, H & L: Day 60. 187

188

3.1

Alveoli per acinus

191

The average entrance ring count, which corresponds to the number of alveoli per acinus for the 125 acini at day 4 is 48 ± 41 alveoli. For the 58 acini at day 10 it is 89 ± 84 alveoli, for the 42 acini at day 21 it

is 233 ± 164 alveoli. At day 60 we assessed 43 acini in total, on average they have 702 ± 219 alveoli.

192

The values for the single animal are given in table 1 and plotted in figure 2.

193

The alveolar number shows highly significant differences (Šidák-corrected p-value < 0.00167 (44)) between all possible combination of days. All possible combinations of entrance ring counts per day are

189 190

194

5

Animal 04A 04B 04C 10A 10B 10C 21B 21D 21E 60B 60D 60E

Assessed acini 51 23 51 27 14 17 14 17 11 24 10 9

Average counts 26.73 65.04 60.51 77.85 84.57 108.76 208.14 196.0 323.09 701.75 668.3 739.11

STD 23.56 43.85 45.42 56.31 65.75 125.45 197.71 128.56 145.94 230.95 121.67 281.22

Minimum 4 15 10 18 23 15 35 50 108 322 444 272

Maximum 111 171 249 245 199 505 781 493 572 1296 810 1204

Table 1: Detailed alveolar numbers for each animal.

Figure 2: Distribution of the number of alveoli per acinus (entrance ring count per acinus) for each animal. Left: linear scale, right: logarithmic scale. The entrance ring counts per day are all significantly different (all p-values better than 1.9×10^{-5} , which is the one between days 4 and 10).

196

significantly different (all p-values are better than $p = 1.9 \times 10^{-5}$, which is the p-value of the difference between days 4 and 10). The entrance ring counts for all animals are independent ($p = 1.6 \times 10^{-34}$).

197

3.2

195

198 199 200 201 202 203 204

Acinus volume

The stereological assessment resulted in a mean acinar volume of $0.03 \pm 0.04 \text{ mm}^3$ for the 125 acini at day 4. For the 58 acini at day 10 we get a volume of $0.04 \pm 0.05 \text{ mm}^3$. For the 42 acini at day 21 a volume of $0.10 \pm 0.09 \text{ mm}^3$ and for the 43 acini at day 60 a volume of $0.74 \pm 0.37 \text{ mm}^3$. The values for the single animals are shown in table 2 and displayed in figure 3. The mean volume of the 20 % smallest acini to the 20 % largest acini at day 4 increases 27.47 times (from $0.0035 \text{ }\mu\text{l}$ to $0.095 \text{ }\mu\text{l}$, $N=25$). At day 10, this increase is 15.28 times (from $0.0071 \text{ }\mu\text{l}$ to $0.11 \text{ }\mu\text{l}$, $N=12$). At day 21, this increase is 14.42 times (from $0.018 \text{ }\mu\text{l}$ to $0.26 \text{ }\mu\text{l}$, $N=8$). At day 60, we saw an increase of 3.94 times (from $0.33 \text{ }\mu\text{l}$

6

Animal 04A 04B 04C 10A 10B 10C 21B 21D 21E 60B 60D 60E

Assessed acini

Average [mm^3]

STD [mm^3]

Minimum [mm^3]

Maximum [mm^3]

51 23 51 27 14 17 14 17 11 24 10 9

0.01 0.06 0.04 0.03 0.03 0.06 0.09 0.11 0.12 0.59 0.89 0.98

0.01 0.05 0.04 0.03 0.03 0.08 0.09 0.11 0.07 0.22 0.35 0.53

0.0 0.01 0.01 0.0 0.0 0.0 0.01 0.01 0.03 0.23 0.36 0.19

0.04 0.19 0.28 0.11 0.1 0.33 0.32 0.38 0.24 1.1 1.58 1.88

Table 2: Detailed volume data (in mm^3) for each animal.

205

to $1.3 \text{ }\mu\text{l}$, $N=9$).

Figure 3: Distribution of the acinar volumes for each animal. Left: linear scale, right: logarithmic scale. The acinar volumes are all significantly different (all p-values better than $4.5e-6$, which is the one between days 10 and 21) for each combination of days except between days 4 and 10 ($p=0.08$). 206 207 208 209 210

The acinar volumes show highly significant differences between all possible combinations of days except between days 4 and 10 ($p=0.08$). All other p-values are better than $p=4.5e-6$, which is the p-value for the difference between days 10 and 21. The statistical analysis is equal to what is briefly described for the entrance ring count above. The acinar volumes for animals 21E and all animals of day 60 are non-normally distributed, but all acinar volumes per animal are independent ($p=5e-29$).

7

211

212 213 214 215

3.3

Alveoli per volume

The mean number of alveoli for the 125 acini at day 4 is 2166 ± 1132 alveoli per mm^3 . For the 58 acini at day 10 we counted 2831 ± 1189 alveoli per mm^3 , for the 42 acini at day 21 2723 ± 771 alveoli per mm^3 and for the 43 acini at day 60 1080 ± 349 alveoli per mm^3 . These numbers were found by dividing the counted entrance rings by the acinus volumes. The numbers for the single animals are shown in table 3 and displayed in figure 4. Animal 04A 04B 04C 10A 10B 10C 21B 21D 21E 60B 60D 60E

Assessed acini 51 23 51 27 14 17 14 17 11 24 10 9

Average [mm^{-3}] 3124 1363 1569 2685 3091 2848 2642 2534 3119 1249 838 898

STD [mm^{-3}] 1152 499 380 1022 1166 1462 493 895 775 297 271 323

Minimum [mm^{-3}] 1618 679 799 1246 1890 1182 1625 1111 1604 530 476 411

Maximum [mm^{-3}] 8208 2704 2775 5582 5422 7009 3344 4032 4379 1912 1221 1463

Table 3: Details of alveolar density (number per mm^3) per acinus volume for each animal.

Figure 4: Number of alveoli per acinus volume. Left: linear scale, right: logarithmic scale. The number of alveoli per acinus volume are all significantly different (all p-values are better than $5e-5$, which is the one between days 4 and 21) for each combination of days except between days 10 and 21 ($p=0.7$). 216 217 218 219

The counts per volume, which correspond to the number of alveoli per acinus volume are a value for estimating the complexity of the single acini. This acinus complexity shows highly significant differences between all possible combinations of days except between days 10 and 21 ($p=0.7$). All other days have a 8

222

p-value better than $p=5e-5$, this being the one between days 4 and 21. The statistical analysis is equal to what is briefly described for the entrance ring count above. The counts per volume for all animals except 04A are non-normally distributed, but all are independent ($p=2.9e-21$).

223

3.4

220 221

Number of acini

229

The number of acini for day 4 was 18260 ± 16555 acini, for day 10 14359 ± 5611 acini, for day 21 11203 ± 2681 acini and for day 60 4277 ± 777 acini. These numbers were obtained by dividing the parenchymal volume of the lungs (10) with the Cavalieri-estimated volume of the acini. To calculate

these data we had to use data of two different studies. Most likely due to error propagation, we observed a large standard deviation. In the end the number of acini do not differ significantly between the days and is not different to the value published by Barre et al. (8).

230

3.5

224 225 226 227 228

Total number of alveoli per lung

235

The total alveolar number for day 4 was found to be 0.64 ± 0.34 million alveoli, for day 10 1.23 ± 0.39 million alveoli, for day 21 2.65 ± 0.57 million alveoli, and for day 60 3.01 ± 0.58 million alveoli. The total number of acini was estimated by dividing the mean parenchymal volume of the lungs (10), by the shrinkage-corrected stereologically estimated acinar volume. The number of alveoli is then simply the multiplication of the average entrance ring count with the estimated number of acini.

236

3.6

231 232 233 234

Volume of individual alveoli

242

The mean volume of one alveolus for day 4 was $686151 \mu\text{m}^3$, for day 10 $452285 \mu\text{m}^3$, for day 21 $445373 \mu\text{m}^3$ and for day 60 $1053526 \mu\text{m}^3$. This corresponds to an average diameter per alveolus of $109 \mu\text{m}$, $95 \mu\text{m}$, $95 \mu\text{m}$, and $126 \mu\text{m}$ for days 4, 10, 21 and 60, respectively. The average volume of one alveolus was estimated by dividing the mean acinar volume by the mean count of alveoli for each day separately. The average diameter was estimated by assuming spherical alveoli and solving the volume equation of a sphere to the diameter.

243

4

237 238 239 240 241

Discussion

258

To our best knowledge, the present manuscript is the first to quantitatively describe the changes in the volumes of single rat lung acini based on stereological analysis of a large number of individual acini. In addition, we can easily estimate the number of acini during lung development from our data and compare this to prior work. There are some limitations to our results though; for technical reasons, we only assessed the acini in the lower medial tip of the right lower lung lobe. However, it was previously shown that the right lower lobe is a valid sample for the entire lung (8) and that

information drawn from one lobe is representative for the whole lung (45). Furthermore, based on stereological data, Zeltner et al. (45) were able to show that the lung parenchyma is quite homogeneous. Looking at individual acini, Kizhakke Puliyakote et al. (21) observed that the peripheral, pleura facing acini possess an acinar volume which is two thirds larger than the volume of the central ones. However, they did not report additional regional differences, e.g. between acini located cranially and caudally. Own preliminary data are indicative for the same result. We imaged an entire rat lung in situ immediately post mortem using high resolution synchrotron radiation based X-ray tomographic microscopy (46). A first analysis of regional difference show similar results as mentioned above. Therefore, we believe that our sample is more than suitable for the drawn conclusions.

259

4.1

244 245 246 247 248 249 250 251 252 253 254 255 256 257

260 261 262 263

Acinus volumes

The mean acinar volume significantly increases during lung development from postnatal days 10 to 60 with all p-values better than 4.5×10^{-6} . No significant difference was observed between postnatal days 4 and 10 ($1.2 \times$ increase, $p=0.08$). A large part of the acinus volume increase happens after day 21 (compare Fig. 3), which is consistent with previous literature (10; 1).

9

264 265 266 267 268 269 270 271 272 273 274 275 276 277 278 279 280 281 282 283 284 285 286

As mentioned in the introduction, Barré et al. (8) have shown that the number of acini remains constant during lung development. This is somewhat surprising since the total lung volume increases by roughly a factor of 11 during alveolarization. Therefore, we expect the mean volume of the acini to increase by at least the same factor (8; 10). We observed that the mean volume of acini increases 22.66 times between days 4 and 60 ($p=1.8 \times 10^{-22}$) which corresponds to an approximately 23 times increase of the total lung volume. The other combinations of increases were: day 4 to day 21: $3.18 \times$ ($p=1.3 \times 10^{-9}$), day 10 to day 21: $2.60 \times$ ($p=4.5 \times 10^{-6}$), day 10 to day 60: $18.46 \times$ ($p=1.4 \times 10^{-17}$), day 21 to day 60: $7.11 \times$ ($p=7.1 \times 10^{-15}$). The increase from day 4 to day 10 was not significant ($p=0.08$) at $1.23 \times$. During the same time, the coefficients of variation of the acinus volumes dropped from 1.26 to 0.49 but the difference between the mean volumes of the fraction of the 20 % smallest and 20 % largest acini decreased from a factor of 27.47 (day 4) to a factor of 3.94 (day 60). This indicates that the dispersion of the value is based on an entirely different pattern of distribution of acinar sizes and that the difference of the mean acinus volumes from the smallest to the largest fraction per day becomes smaller and smaller during postnatal lung development. When comparing the acinus volumes normalized to the largest volume per day, we found that the volumes are closer together on day 4 and are spread out more on the other days (Fig. 5). Additionally, at days 4, 10 and 21 the distribution of the normalized volumes is skewed towards below the average (median of normalized volumes at day 4: 0.16, at day 10: 0.18 and at day 21: 0.23), which means that we have more smaller than larger acini early in the development. At day 60, the distribution is more homogeneous, with the median of the normalized acinus volumes at exactly 0.50. This result let us speculate that acinar growth is not constant during lung development. It seems that some acini increase their volume faster than others. As a result we speculate that an increased percentage of acini is somehow dormant at day 4-21, while at day 60 most of the acini reached their final volume.

Figure 5: Normalized acinar volumes. The spread of the volumes is small early in the development and skewed towards the lower end of the volumes. At day 60, the median is exactly in the middle of the normalized volumes. 287 288 289 290

By dividing the parenchymal volumes of each lung estimated by Tschanz et al. (Table 1, (10)) by the mean number of acini estimated by Barré et al. (9) we can estimate the mean acinar volume for each day. The acinus volume we estimated by point counting (Cavalieri estimation) are on average 2.07 times lower 10

299

but show a similar increase over the studied period (data shown in supplementary Fig. 7). It appears that the comparison between data obtained by stereology based on classical paraffin sections or on any kind of 3D-imaging has its limitation if it comes to the absolute numbers. First, due to the coast of Britain-effect the exact value of every surface measurement is depending on the resolution of the imaging method (47). Second, the thickness of the alveolar septa in 3D-imaging data is heavily depending on the segmentation between airspace and tissue - regardless if it is done manually or by a computed algorithm. We observed that the airspace volumes obtained by 3D-imaging has a tendency to be smaller than the ones determined using classical paraffin sections. However, the relative numbers obtained in one study match the ones of other studies quite well.

300

4.2

291 292 293 294 295 296 297 298

301 302 303 304 305 306 307

Acinus complexity, alveoli per volume

The volume and shape of the alveoli, alveolar ducts, and the acini are critical parameters for ventilation and particle deposition (48; 49; 50). Particle deposition, for example, is relatively low during the first two weeks of a rats' life, high at postnatal day P21 and medium at days P36-P90 (13; 12). This correlates well with our results, where we found a significantly larger acinus complexity (number of alveoli per acinus volume) at days 10 and 21 compared to days 4 and 60 (p-values all better than 5.4×10^{-5} , which is the one for day 4 vs. day 21). Kreyling et al. (13) report a maximal retention of gold nanoparticles at this time point (see their Fig. 1).

313

Tschanz et al. (10) stereologically estimated the mean total acinar volume as the sum of ductal and alveolar air spaces. The mean volume of the individual alveoli was found to be smallest around postnatal day 21 (see their Fig. 4). We thus postulate a high acinar complexity at days 10 and 21 while early and late in the lung development, the acinar complexity is relatively low. This also correlates with structural changes. In rats, the alveolar air spaces are large during the first two weeks of life, small at day P21 and medium afterward (10).

314

4.3

308 309 310 311 312

Number of acini

317

Previously, it was shown that the number of acini remains constant during postnatal lung development from day 4 to 60 (8), with a mean of 5612 ± 547 acini per lung. Based on the acinar and parenchymal volume we calculated the number of acini and were able to verify the previously reported result.

318

4.4

315 316

319 320 321 322 323 324

Total alveolar number

In this study, we assessed the number of alveoli per acinus. The alveolar number we get (0.64 ± 0.34 , 1.23 ± 0.39 , 2.65 ± 0.57 , 3.01 ± 0.58 million alveoli for days 4, 10, 21 and 60, respectively) have to be seen in the context of the results shown by Tschanz et al. (0.823 ± 0.01 , 3.538 ± 1.26 , 14.303 ± 3.08 and 19.297 ± 3.06 million alveoli, (10), Table 1). On average, our results are five times smaller but show the same trend when linearly corrected with a factor of 5.04. The values from Tschanz et al. overlap well with our linearly scaled values, as seen in Fig. 6.

333

As shown in a study of Osmanagic et al. (51) the total alveolar number shows a large variability between different labs. E.g. the reported total number of alveoli in adult C57BL6 mice differs by a factor of approximately 8. These studies were all performed in labs well-known for their quality of stereology-based investigations of lung morphology. Therefore, any simple bias or methodical error may not account for the reported differences. It seems to be that the total number of alveoli is dependent on unknown small methodical differences. However, the relative numbers are surely reliable, especially, if the comparison is done in groups of animals processed in parallel and counted by the same operator. We assessed the same lungs as Tschanz et al. (10), but based on a very different imaging method and with two different persons performing the stereological assessment. The latter two points may explain the factor of 5.04.

334

4.5

325 326 327 328 329 330 331 332

335 336

Volumes of individual alveoli

By dividing the alveolar air space by the number of alveoli we can estimate a mean alveolar volume of $5.91 \text{e}5 \mu\text{m}^3$ for day 4, of $2.49 \text{e}5 \mu\text{m}^3$ for day 10, of $1.34 \text{e}5 \mu\text{m}^3$ for day 21, and $2.93 \text{e}5 \mu\text{m}^3$ for day 60.

Figure 6: Number of alveoli based on data from Tschanz et al. (10) together with our linearly scaled data (our data multiplied by 5.04). Values are plotted with a band of the width of their standard deviation.

341

On average, our values are 2.48 times larger than the volumes of the single alveoli as calculated from data shown in Table 1 of Tschanz et al. (10) (day 4: $6.87 \times 10^5 \mu\text{m}^3$, day 10: $4.52 \times 10^5 \mu\text{m}^3$, day 21 $4.45 \times 10^5 \mu\text{m}^3$ and day 60 $1.05 \times 10^6 \mu\text{m}^3$), but scale equally during postnatal lung development. Tschanz et al. estimated the total alveolar volume without the alveolar ducts. Since we directly estimated the volume fraction of the alveoli per acinus our number is actually expected to be larger.

342

4.6

337 338 339 340

343 344 345 346 347 348 349 350 351 352 353 354

Physiological relevance of the acinar size

It has been predicted by computational fluid dynamics simulations and by to-scale experiments that the amount and location of massless particle deposition, as well as ventilation are depending on the size of the acini. The predictions could be confirmed at least in one case, where mice received fluorescent particles during mechanical ventilation. In 3D-visualizations the particles were predominately detected in the proximal half of the acini (52). Based on the above-mentioned knowledge and the data of this study, we propose the following. In very small acini as the smallest ones we observed at postnatal day 4 acinar flows are mainly characterized by radial streamlines. Massless particle deposition is governed by diffusion (53). As the acini increase in size, convective transport becomes more and more dominant in the proximal regions of the acini. In larger acini, the proximal region shows a much higher particle retention than the distal once. The proximal regions may even be viewed analogous to a filter capturing the particles whereas the distal regions do not receive significant amounts (14; 16; 54).

361

Multi-breath gas-washout is also dependent on the size of the acini. Based on computational simulations of nitrogen multi-breath gas-washout it has been shown that small acini washout faster at the beginning and slower at the end of the washout as compared to larger acini (15). Not surprisingly, the distribution of the acinar sizes in terms of their range has also an influence on the gas-washout. Furthermore, a clustering versus an even distribution of the locations of acinar similar sizes effects gas-washout. Therefore, the question where an acinus of which size is located in the lungs has a significant influence on pulmonary ventilation and particle deposition.

362

The larger distribution of the acinar sizes at day 4 as compared to day 60 let us speculate what this

355 356 357 358 359 360

363 364 365 366 367 368

may mean biologically. Physiologically, a larger distribution implies a less homogeneous ventilation and an increased gas-washout time. Therefore, the decrease of the inhomogeneity of the acinar sizes may be understood as an optimization of gas-exchange in adult animals. The consideration of the location is not only a theoretical consideration, because it has been shown in adult mice that the acini close to the pleura are larger than central ones (21). Therefore, acini of different size are not evenly distributed in the lungs.

371

To our best knowledge, very few data characterizing acinar properties was available up to now. This is especially true for lung development. Therefore, the data of the hereby presented study can contribute to the improvements of computational simulations of pulmonary ventilation and particle deposition.

372

5

369 370

Conclusion

380

We conclude that our method is well suited to efficiently extract precise qualitative and quantitative values of large amounts of single acini from non-destructive three-dimensional tomographic data sets. The underlying stereological analysis can be efficiently performed on tomographic data sets, the analysis of the stereological data was performed in a reproducible manner. Besides, our method enabled us to maximize the number of investigations per sample, thus reducing the number of sacrificed animals. We conclude that newly formed acini show a large size distribution which is reduced by a factor of 7 until adulthood. Most likely the latter leads to a more homogeneous ventilation of the lung and an increase of gas-washout which is equal to a decreased in the number of breaths needed for gas-washout.

381

6

373 374 375 376 377 378 379

Acknowledgments

385

We thank Mohammed Ouanella and Bettina de Breuyn for expert technical assistance. Federica Marone and Bernd Pinzer were of paramount importance with their support at the TOMCAT beamline. Fluri Wieland was of great help with the statistical analysis. We are thankful for the support by the Swiss National Science Foundation (grants 310030_153468 and 310030_175953).

386

382 383 384

Contributions

390

JS conceived the project. DH, SB and JS performed the tomographic data acquisition. DH segmented the acini. EY and DH analyzed the acini stereologically. DH, ST, TC and JS analyzed the data. DH wrote the manuscript and generated all the figures. ST and JS contributed to writing, all authors proof-read the manuscript.

391

8

392

No conflicts of interest, financial or otherwise, are declared by the authors.

393

9

387 388 389

Disclosures

Supplementary figures

13

Figure 7: Plot of the mean acinar volumes. By dividing the parenchymal volumes of each lung estimated by Tschanz et al. (Table 1, (Tschanz 2014)) by the mean number of acini estimated by Barré et al. (9) we can estimate the mean acinar volume for each measured time point (blue plot). We assessed the volumes of the acini by point counting (Cavalieri estimation, orange plot). Our volumes of the acini are on average 2.07 times lower but show a similar increase over the studied period. While the estimation based on Tschanz et al. is from the entire right middle lobe and on Barré et al. globally for the whole organ, our estimation is solely based on the stereological analysis of the acini in the lower medial tip of the right lower lung lobe.

Figure 8: Plot of the estimated number of acini. The blue plot shows our estimation, based on the division of the parenchymal volume by the average volume of the acini. The orange plot is based on the data shown by Barre et al. (9; 8).

394

395 396 397 398 399 400 401

[Online].

<https://gist.github.com/habi/>

39. Amrhein V, Greenland S, McShane B. Scientists rise up against statistical significance. *Nature* 567: 305–307, 2019.

40. Barré SF, Haberthür D, Cremona TP, Stampanoni M, Schittny JC. The total number of acini remains constant throughout postnatal rat lung development. *American Journal of Physiology-*

14

402

Lung Cellular and Molecular Physiology 311: L1082–L1089, 2016.

403

9. Barré SF, Haberthür D, Stampanoni M, Schittny JC. Efficient estimation of the total number of acini in adult rat lung. *Physiological Reports* 2: e12063, 2014.

404 405 406 407 408 409 410 411 412 413 414 415 416

46. Borisova E, Lovric G, Miettinen A, Fardin L, Bayat S, Larsson A, Stampanoni M, Schittny JC, Schlepütz CM. Micrometer-resolution X-ray tomographic full-volume reconstruction of an intact post-mortem juvenile rat lung.. *Histochem Cell Biol.* .

47. Burri PH, Dbaly J, Weibel ER. The postnatal growth of the rat lung. I. Morphometry. *The Anatomical Record* 178: 711–730, 1974.

48. CRUZ-ORIVE LM. Precision of Cavalieri sections and slices with local errors. *Journal of Microscopy* 193: 182–198, 1999.

49. Cruz-Orive LM. Precision of Cavalieri sections and slices with local errors. *Journal of Microscopy* 193: 182–198, 1999.

50. Erhardt W, Kölle P, Henke J, Haberstroh J, Baumgartner C, Tacke S. *Anästhesie und Analgesie beim Klein-und Heimtier: mit Exoten, Labortieren, Vögeln, Reptilien, Amphibien und Fischen*. Schattauer Verlag, 2012.

418

14. Fishler R, Hofemeier P, Etzion Y, Dubowski Y, Sznitman J. Particle dynamics and deposition in true-scale pulmonary acinar models. *Scientific Reports* 5, 2015.

419

24. Flecknell P. Replacement, reduction and refinement.. *ALTEX* 19: 73–8, 2002.

420

32. Haberthür D, Barre SF, Tschanz SA, Yao E, Stampanoni M, Schittny JC. Visualization and stereological characterization of individual rat lung acini by high-resolution X-ray tomographic microscopy. *Journal of Applied Physiology* 115: 1379–1387, 2013.

417

421 422

28. Haberthür D, Hintermüller C, Marone F, Schittny JC, Stampanoni M. Radiation dose optimized lateral expansion of the field of view in synchrotron radiation X-ray tomographic microscopy. *Journal of Synchrotron Radiation* 17: 590–599, 2010.

38. Haberthür D. habi/acinar-analysis: Zenodo. .

23. Haberthür D, Barré SF, Tschanz SA, Yao E, Stampanoni M, Schittny JC. Visualization and stereological characterization of individual rat lung acini by high-resolution X-ray tomographic microscopy. *Journal of Applied Physiology* 115: 1379–1387, 2013.

428 429 430 431 432 433 434 435 436 437 438 439 440 441 442 443 444 445

6. Haefeli-Bleuer B, Weibel ER. Morphometry of the human pulmonary acinus. *The Anatomical Record* 220: 401–414, 1988.
7. Hasler D, Anagnostopoulou P, Nyilas S, Latzin P, Schittny J, Obrist D. A multi-scale model of gas transport in the lung to study heterogeneous lung ventilation during the multiple-breath washout test. *PLOS Computational Biology* 15: e1007079, 2019.
8. Henry FS, Haber S, Haberthür D, Filipovic N, Milasinovic D, Schittny JC, Tsuda A. The Simultaneous Role of an Alveolus as Flow Mixer and Flow Feeder for the Deposition of Inhaled Submicron Particles. *Journal of Biomechanical Engineering* 134: 121001, 2012.
9. Hofemeier P, Sznitman J. Role of Alveolar Topology on Acinar Flows and Convective Mixing. *Journal of Biomechanical Engineering* 136, 2014.
10. Hsia CC, Hyde DM, Ochs M, Weibel ER. An official research policy statement of the American Thoracic Society/European Respiratory Society: standards for quantitative assessment of lung structure.. *Am J Respir Crit Care Med* 181: 394–418, 2010.
11. Hsia CCW, Hyde DM, Ochs M, Weibel ER. An Official Research Policy Statement of the American Thoracic Society/European Respiratory Society: Standards for Quantitative Assessment of Lung Structure. *American Journal of Respiratory and Critical Care Medicine* 181: 394–418, 2010.

446 447 448 449 450 451 452 453 454 455 456 457 458 459 460 461 462 463 464 465 466 467 468 469
470 471 472 473 474 475 476 477 478 479

33. Hyde DM, Tyler NK, Putney LF, Singh P, Gundersen HJ. Total number and mean size of alveoli in mammalian lung estimated using fractionator sampling and unbiased estimates of the Euler characteristic of alveolar openings.. *Anat Rec A Discov Mol Cell Evol Biol* 277: 216–26, 2004.
34. Kauffman SL, Burri PH, Weibel ER. The postnatal growth of the rat lung II. Autoradiography. *The Anatomical Record* 180: 63–76, 1974.
35. Kluyver T, Ragan-Kelley B, Pérez F, Granger B, Bussonnier M, Frederic J, Kelley K, Hamrick J, Grout J, Corlay S, Ivanov P, Avila D, Abdalla S, Willing C. Jupyter Notebooks – a publishing format for reproducible computational workflows. In: *Positioning and Power in Academic Publishing: Players, Agents and Agendas*, edited by Loizides F, Schmidt B. IOS Press, 2016, p. 87–90.
36. Kreyling WG, Möller W, Holzwarth U, Hirn S, Wenk A, Schleh C, Schäffler M, Haberl N, Gibson N, Schittny JC. Age-Dependent Rat Lung Deposition Patterns of Inhaled 20 Nanometer Gold

Nanoparticles and their Quantitative Biokinetics in Adult Rats. ACS Nano 12: 7771–7790, 2018.

37. Kruskal WH, Wallis WA. Use of Ranks in One-Criterion Variance Analysis. Journal of the American Statistical Association 47: 583–621, 1952.

38. Mandelbrot B. How Long Is the Coast of Britain? Statistical Self-Similarity and Fractional Dimension. Science 156: 636–638, 1967.

39. Mann HB, Whitney DR. On a Test of Whether one of Two Random Variables is Stochastically Larger than the Other. The Annals of Mathematical Statistics 18: 50–60, 1947.

40. Marone F, Hintermüller C, McDonald S, Abela R, Mikuljan G, Isenegger A, Stampanoni M. X-ray Tomographic Microscopy at TOMCAT. Journal of Physics: Conference Series 186: 012042, 2011.

41. Marone F, Mokso R, Fife JL, Irvine S, Modregger P, Pinzer BR, Mader K, Isenegger A, Mikuljan G, Stampanoni M. Synchrotron-based X-ray Tomographic Microscopy at the Swiss Light Source for Industrial Applications. Synchrotron Radiation News 24: 24–29, 2011.

43. Mercer RR, Crapo JD. Three-dimensional reconstruction of the rat acinus.. J Appl Physiol 63: 785–94, 1987.

51. Osmanagic E, Sukstanskii AL, Quirk JD, Woods JC, Pierce RA, Conradi MS, Weibel ER, Yablonskiy DA. Quantitative assessment of lung microstructure in healthy mice using an MRbased 3He lung morphometry technique. Journal of Applied Physiology 109: 1592–1599, 2010.

52. Puliyakote ASK, Vasilescu DM, Newell JD, Wang G, Weibel ER, Hoffman EA. Morphometric differences between central vs. surface acini in A/J mice using high-resolution micro-computed tomography. Journal of Applied Physiology 121: 115–122, 2016.

53. Rodriguez M, Bur S, Favre A, Weibel ER. Pulmonary acinus: Geometry and morphometry of the peripheral airway system in rat and rabbit. American Journal of Anatomy 180: 143–155, 1987.

481

40. SHAPIRO SS, WILK MB. An analysis of variance test for normality (complete samples). Biometrika 52: 591–611, 1965.

482

3. Schittny JC. Development of the lung. Cell and Tissue Research 367: 427–444, 2017.

483

4. Schittny JC. How high resolution 3-dimensional imaging changes our understanding of postnatal lung development. Histochemistry and Cell Biology 150: 677–691, 2018.

480

484 485 486 487 488 489 490

5. Schittny JC, Mund SI, Stampanoni M. Evidence and structural mechanism for late lung alveolarization. American Journal of Physiology-Lung Cellular and Molecular Physiology 294: L246–L254, 2008.

6.

7. Semmler-Behnke M, Kreyling WG, Schulz H, Takenaka S, Butler JP, Henry FS, Tsuda A. Nanoparticle delivery in infant lungs. Proceedings of the National Academy of Sciences 109: 5092–5097, 2012.

491 492 493 494 495 496 497 498 499 500 501 502 503 504 505 506 507 508 509 510 511 512 513 514
515 516 517 518 519 520 521 522 523 524 525 526 527 528 529 530 531 532 533 534

34. Sterio DC. The unbiased estimation of number and sizes of arbitrary particles using the disector. [Online]. *Journal of microscopy* 134: 127–36, 1984. <http://dx.doi.org/10.1111/j.1365-2818.1984.tb02501.x>.
35. Storey WF, Staub NC. Ventilation of terminal air units. *Journal of Applied Physiology* 17: 391–397, 1962.
36. Sznitman J. Convective gas transport in the pulmonary acinus: Comparing roles of convective and diffusive lengths. *Journal of Biomechanics* 42: 789–792, 2009.
37. Sznitman J, Heimsch F, Altorfer D, Schittny JC, Rösgen T. Alveolar flow simulations during rhythmical breathing motion in reconstructed XTM acinar airspaces. *Journal of Biomechanics* 39: S441, 2006.
38. Sznitman J, Sutter R, Altorfer D, Stampanoni M, Rösgen T, Schittny JC. Visualization of respiratory flows from 3D reconstructed alveolar airspaces using X-ray tomographic microscopy. *Journal of Visualization* 13: 337–345, 2010.
39. TSCHANZ SA, BURRI PH, WEIBEL ER. A simple tool for stereological assessment of digital images: the STEPanizer. *Journal of Microscopy* 243: 47–59, 2011.
40. Tschanz SA, Salm LA, Roth-Kleiner M, Barré SF, Burri PH, Schittny JC. Rat lungs show a biphasic formation of new alveoli during postnatal development. *Journal of Applied Physiology* 117: 89–95, 2014.
41. Tsuda A, Filipovic N, Haberthür D, Dickie R, Matsui Y, Stampanoni M, Schittny JC. Finite element 3D reconstruction of the pulmonary acinus imaged by synchrotron X-ray tomography. *Journal of Applied Physiology* 105: 964–976, 2008.
42. Vasilescu DM, Gao Z, Saha PK, Yin L, Wang G, Haefeli-Bleuer B, Ochs M, Weibel ER, Hoffman EA. Assessment of morphometry of pulmonary acini in mouse lungs by nondestructive imaging using multiscale microcomputed tomography. *Proceedings of the National Academy of Sciences* 109: 17105–17110, 2012.
43. Vasilescu DM, Klinge C, Knudsen L, Yin L, Wang G, Weibel ER, Ochs M, Hoffman EA. Stereological assessment of mouse lung parenchyma via nondestructive multiscale micro-CT imaging validated by light microscopic histology. *Journal of Applied Physiology* 114: 716–724, 2013.
44. Virtanen P, Gommers R, Oliphant TE, Haberland M, Reddy T, Cournapeau D, Burovski E, Peterson P, Weckesser W, Bright J, van der Walt SJ, Brett M, Wilson J, Millman KJ, Mayorov N, Nelson ARJ, Jones E, Kern R, Larson E, Carey CJ, Polat İ, Feng Y, Moore EW, VanderPlas J, Laxalde D, Perktold J, Cimrman R, Henriksen I, Quintero EA, Harris CR, Archibald AM, Ribeiro AH, Pedregosa F, van Mulbregt P, Contributors SP1. 0. SciPy 1.0–Fundamental Algorithms for Scientific Computing in Python. 2019.
45. Woodward JD, Maina JN. A 3D digital reconstruction of the components of the gas exchange tissue of the lung of the muscovy duck *Cairina moschata*. *Journal of Anatomy* 206: 477–492, 2005.
46. Yang L, Feuchtinger A, Möller W, Ding Y, Kutschke D, Möller G, Schittny JC, Burgstaller G, Hofmann W, Stoeger T, Razansky D, Walch A, Schmid O. Three-Dimensional Quantitative Co-Mapping of Pulmonary Morphology and Nanoparticle Distribution with Cellular Resolution in Nondissected Murine Lungs. *ACS Nano* (January 2019). doi: 10.1021/acsnano.8b07524.
47. Zeltner TB, Bertacchini M, Messerli A, Burri PH. Morphometric estimation of regional differences in the rat lung.. *Exp Lung Res* 16: 145–58, 1990.
48. Šidák Z. Rectangular Confidence Regions for the Means of Multivariate Normal Distributions. *Journal of the American Statistical Association* 62: 626–633, 1967.

References
